glacies

MDPI

Article

Characterising Ice Motion Variability at Helheim Glacier Front from Continuous GPS Observations

Christopher Pearson [1], James Colinese [2], Tavi Murray [2,*] and Stuart Edwards [1]

[1] School of Engineering, Newcastle University, Newcastle upon Tyne NE1 7RU, UK; chr1spears0n@hotmail.com (C.P.); stuart.edwards@newcastle.ac.uk (S.E.)
[2] Department of Geography, Swansea University, Swansea SA2 8PP, UK; jcolinese@gmail.com
* Correspondence: t.murray@swansea.ac.uk or tavimurray8@gmail.com

Abstract

Understanding short-term glacier motion is vital for assessing ice sheet dynamics in a warming climate. This study investigates the tidal and diurnal influences on the flow of Helheim Glacier, one of Greenland's fastest-flowing marine-terminating glaciers, using data from 18 high-frequency GPS sensors and a regional tide gauge collected during summer 2013. A Kalman filter was applied to separate and quantify glacier velocity, tidal admittance, and diurnal melt-driven acceleration. Results reveal a high level of tidal admittance affecting the horizontal flow speed of the glacier, especially at the centre of the glacier, which is propagated upstream. This admittance corresponds to a 0.38–0.68 m/day reduction from the mean at high spring tide and a comparable increase at low tide. The glacier's vertical motion showed strong tidal control close to the terminus, of 0.6–1.05 m during high spring tides, but this was significantly reduced more than 1 km from the terminus. Diurnal variations in horizontal speed are less spatially and temporally variable, with most nodes experiencing changes from a mean speed of ±0.1–0.3 m/day. These findings demonstrate that both tidal forcing and meltwater input to the basal system exert a significant, and potentially spatially variable, control on glacier dynamics, highlighting the need to incorporate short-period external forcing into predictive models of marine-terminating glacier behaviour.

Keywords: marine-terminating glacier; tidewater glacier; glacier dynamics; GPS

1. Introduction

The dynamics of marine-terminating glaciers are governed by the balance between gravitational driving stresses and resistive stresses [1] (pp. 2318–2337), [2] (pp. 77–89). Variation in external factors makes these dynamics challenging to predict, especially close to the front margin. Factors such as ocean tide level fluctuations affect the motion of the glacier front, submarine melt can impact glacier calving, and surface melt causes pressure variations beneath the glacier [2] (pp. 77–89), [3,4] (pp. 119–128), [5] (pp. 2925–2941). Periodic changes in glacier flow speed, driven by the tides, have been documented at numerous glaciers worldwide, including Helheim Glacier [6] (pp. 1169–1180), [7] (pp. 1375–1384), [8,9] (pp. 587–598). However, variations in flow speed have also been linked to other factors, including meltwater inputs [6] (pp. 1169–1180) and seasonal changes in calving front position [10] (pp. 759–770). As a result, isolating the impact of each individual influence acting on a glacier is often difficult, complicating efforts to determine their specific contributions to glacier motion.

Academic Editor: Steven R. Fassnacht

Received: 7 October 2025
Revised: 15 December 2025
Accepted: 24 December 2025
Published: 7 January 2026

The Greenland ice sheet is the largest ice sheet in the Northern Hemisphere and is an important contributor to sea-level rise, due to accelerating mass loss through changes in surface mass balance and iceberg calving from its marine-terminating glaciers [11]. Helheim Glacier (Figure 1), one of Greenland's largest marine-terminating glaciers, drains an area of approximately 52,000 km^2 of the Greenland Ice Sheet [12] (pp. 964–982) and terminates in Sermilik Fjord. This glacier has been extensively studied in previous research, including [6] (pp. 1169–1180), [13,14] (pp. 301–308), [15,16] (pp. 3926–3931). The glacier's flow speed can be up to 25 m/day [14] (pp. 301–308), [17], and it has a calving front spanning roughly 6 km in width. The glacier front has varied in position, with a major retreat of ~6 km [18] occurring 2000–2005, followed by stabilisation and a subsequent re-advance during 2006–2007. The retreat event was seen synchronously across many marine-terminating glaciers in SE Greenland and has been suggested to be controlled by regional ocean warming [19] (pp. 986–990), [20]. During 2011–2015, the front of Helheim Glacier remained relatively stable, advancing and retreating ~3–4 km, with indications of seasonal variability [21] (pp. 47–53).

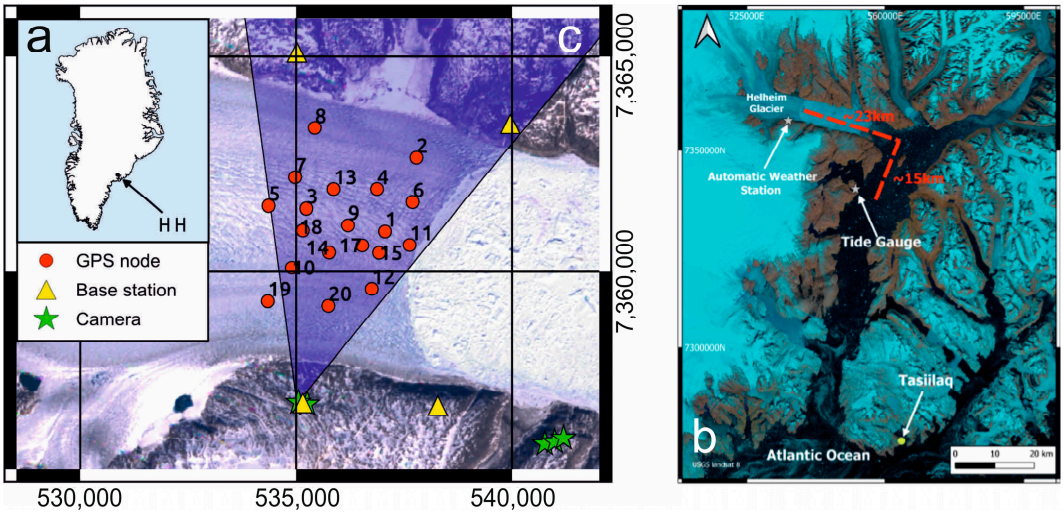

Figure 1. (**a**) Location of Helheim Glacier (HH) in Greenland. (**b**) Location of the tide gauge, deployed by Fiammetta Straneo (University of California, San Diego) [22] in Sermilik Fjord in 2011 and recovered in 2013. (**c**) Starting positions of the GPS Nodes shown by red dots numbered 1–20; note that Node 16 is missing as it never communicated it's position to a base station. The Grid is UTM zone 24, in metres. Also shown are the locations of the logging base stations and field cameras, which were used to monitor calving from the glacier margin. Adapted from [12].

Iceberg calving at Helheim has been shown to generate glacial earthquakes when the glacier front is lightly grounded and to cause major changes to the front dynamics [23] (pp. 622–624), [24,25] (pp. 305–308). Glacial earthquakes have been detected at Helheim Glacier every year since 1996 using signals recorded on the global seismographic network, but the number of events reported has varied significantly from year to year [26] (pp. 1756–1758), [27,28]. For example, Helheim was reported to have produced only one glacial earthquake in 2011, but this increased to seven in 2012 and nine in 2013 [27] (pp. 1077–1089). During this period, the calving front remained relatively stable until late 2013–2014, when the glacier advanced approximately 3 km into the fjord [21] (pp. 47–53), [29] (pp. 1635–1652).

Alongside the major dynamic drivers resulting from glacier calving, marine-terminating glacier ice dynamics are governed by a combination of tidal forcing and forcing from surface meltwater input into a seasonally-varying basal hydrological system [30] (pp. 609–620), [31] (pp. 525–540). At Helheim Glacier, during the melt season, surface meltwater reaches the

glacier bed rapidly, causing diurnal velocity variations that are strongest near the terminus and decay inland [2] (pp. 77–89). Although increases in meltwater input cause only modest relative speed-ups, the absolute flux change is significant due to the glacier's high baseline velocity [2] (pp. 77–89). Calving events seem able to disrupt the glacier's basal drainage system, enhancing its sensitivity to tidal and surface forcing as well as causing short-term accelerations [17]. Observation of a supraglacial lake drainage similarly showed a short-term acceleration, but no long-term increase in ice discharge occurred [15] (pp. 6065). Taken together, these processes reveal Helheim to be a glacier that is highly responsive to short-term hydrological forcing, but that is buffered against longer-term destabilisation by having a resilient subglacial drainage network.

In the summer of 2013, GPS data were collected at Helheim Glacier using 18 individual GPS nodes installed directly on the glacier's surface (although 20 nodes were installed, one never started collecting data, and one produced no usable data). These nodes transmitted their data via a wireless network to four logging stations positioned on bedrock adjacent to the glacier [16] (pp. 3926–3931), ensuring data retention even if some nodes were lost during iceberg calving events. The results from these sensors have already been used to detail the mechanics of glacier calving at Helheim's front margin [12] (pp. 964–982), [25] (pp. 305–308). Calving at the glacier results from buoyancy-driven flexure initiated at basal crevasses [12] (pp. 964–982). Calving of the backward rotating icebergs that result has been shown to be the cause of glacial earthquakes. In this paper, we use the same data to investigate the longer-term dynamics of the glacier between calving events and aim to differentiate between tidal and non-tidal controls on the glacier's flow speed.

2. Data and Methods

We developed and deployed a wireless GPS network of which 18 on-ice nodes collected data near the margin of Helheim Glacier (Figure 1c; full details are given in [16] (pp. 3926–3931) and [25] (pp. 305–308). The on-ice nodes were placed in position from a helicopter, and although a regular grid of instruments was planned, the realities of heavy crevassing and water on the glacier surface meant the actual network had to deviate from this plan. The initial node placements are shown in Figure 1. Each GPS node transmitted data to one of 4 logging stations situated on nearby bedrock. The nodes were installed between day of year (DOY) 192 and 196 (11–15 July) 2013, and the site was revisited on DOY 240 (28 August) 2013 to recover remaining units. GPS data were recorded at irregular intervals, averaging between 4 and 7 s per epoch. Data coverage and quality vary between nodes as some were lost during calving events at the glacier's front. In total, 5 nodes survived and were collected at the end of the season, although not all 5 collected usable data throughout the entire season.

Tide gauge data for the region were collected by Fiammetta Straneo from the University of California, San Diego [22], over a period of approximately three years, concluding on DOY 235 in 2013. The pressure gauge used for these tide gauge measurements was located about 23 km southeast of Helheim Glacier (Figure 1b) and recorded data at 15-min intervals. Comparisons with a previous tide gauge located in the same location with the AOTIM-5 tidal model found phase agreement within 3 min and amplitude consistency at the centimetre level [6] (pp. 1169–1180), [17].

Each GPS node captured dual-frequency GPS data, which, when processed in conjunction with a local GPS base station, provided potential positioning accuracy of approximately 1–2 cm horizontally and 2–5 cm vertically [16] (pp. 3926–3931). To achieve kinematic positions, the GPS data were processed using Track (GAMIT v10.5) carrier-phase relative positioning from the GAMIT-GLOBK10.50 GPS Processing software created by [32]. The starting locations of each node can be seen in Figure 1c.

The processed GPS positions were separated into plan and vertical components to facilitate independent analysis of potential directional variations in glacier movement. Plan coordinates were transformed into along-track displacements based on the average bearing at each node. Average glacier flow was along a bearing of approximately 110°. Both the along-track displacement and the elevation data were subsequently processed and analysed separately.

Although GPS data theoretically enables centimetre-level accuracy, this level of precision was not achievable due to the environmental conditions. In addition to conventional sources of error—such as ionospheric and tropospheric delays and satellite orbit inaccuracies—more localised issues further compromised positional accuracy. The glacier's uneven surface, marked by large crevasses, and its high-latitude location contributed to pronounced multipath effects and suboptimal satellite geometry. These factors degraded the reliability of GPS positioning. Additionally, because the on-ice instruments were placed directly on the ice surface, they were subjected to lowering as the ice melted, including the possibility of non-uniform melt. This could cause a node's antenna to be non-optimally located, degrading the GPS data, and could lead to non-glacially-caused lateral movements, potentially in any direction, if the instrument slipped on the ice. To reduce the impact of these errors and to smooth the data for identification of long-term trends, a Kalman filter was implemented for post-processing.

The Kalman filter [33] (pp. 35–45) operates using a two-pass smoothing approach. In the first pass, the filter proceeds forward through each epoch, generating preliminary estimates of the state variables. In the second pass, the filter runs in reverse, beginning from the final state vector and associated variance-covariance matrix obtained during the forward pass. This bidirectional filtering process improves the reliability of the final estimates, particularly at the beginning of the time window, where initial (*a priori*) uncertainties may have been higher.

2.1. Along Track Filter

To separately quantify how the glacier's motion is modified by different factors, the Kalman filter was implemented with a functional model incorporating three key parameters [6] (pp. 1169–1180). The first parameter represents the average daily velocity of the glacier, which varied spatially between nodes, ranging from approximately 17 to 25 m/day. The second parameter quantifies how the flow speed is modulated by oceanographic tidal forcing via the tidal admittance, which is defined as the ratio of glacier velocity to tidal forcing [34] (pp. 8969–8975). The third parameter captures daily variations in glacier velocity, assumed to be primarily driven by surface meltwater.

Both the tidal admittance and diurnal amplitude parameters quantify cyclic effects linked to the phases of the tide and solar cycle, respectively. As such, it was necessary to determine the initial phase offset for each to accurately represent the temporal variations in glacier motion. To identify the optimal phase offsets, initial tests were conducted by evaluating all possible offsets in 5-min increments. Correlation analysis was then used to identify the best-fit phase for each parameter.

The functional model for the Kalman Filter is, therefore, a function of the along track position (A_L in metres), the glacier velocity (V in metres/day), the tide height (T in metres) along with its phase offset (T_{off} in seconds), the admittance (A_D unitless), the diurnal amplitude (D_A in metres/day), and its associated phase offset (D_{off} in seconds). The Kalman filter runs at 1 s intervals (whether there is data available at that interval or not), and the subscript i is used for position within the Kalman filter. Note that 86,400 is the number of seconds in a day.

$$A_L(i) = A_L(i-1) + V/86{,}400 - (T(i + T_{off})\, A_D/86{,}400) - (D_A \sin(i + D_{off})/86{,}400) \quad (1)$$

During the initialisation phase of the Kalman filter, the initial glacier velocity is estimated by averaging the displacement over the first 24 h period for each node. Initial values for the tidal admittance and diurnal amplitude parameters are set to 0.3 and 0.2 m/day, respectively, based on iterative refinement. These parameters, however, are not tightly constrained, with initial variances assigned as 0.1 $(m/day)^2$ for velocity (V) and 0.4 for tidal admittance (A_D) and 0.4 $(m/day)^2$ for diurnal amplitude (D_A), allowing the filter to adaptively refine these estimates as additional data are assimilated. As the filter progresses through the dataset, the three parameters are more tightly constrained between epochs by introducing only minimal process noise, reflecting the assumption that these parameters exhibit limited variability and do not change rapidly over time.

2.2. Height Filter

The GPS-derived height of each node was also filtered and analysed to investigate potential variations in vertical glacier motion. The Kalman filter functional model was formulated analogously to that used for the along-track displacement, incorporating the same three key parameters: vertical velocity, tidal admittance, and diurnal amplitude, as defined in Equation (1). The phase offset values for tidal admittance and diurnal amplitude were adopted directly from the along-track analysis, ensuring temporal consistency across components.

Initial values for vertical velocity were set to zero, reflecting the possibility of both uplift and subsidence over time. Similarly, the diurnal amplitude was initialised at zero, as diurnal effects were not anticipated to exert a substantial influence on vertical displacement. Tidal admittance, however, was initialised at 0.3, accounting for the glacier's potential to undergo vertical oscillations in response to tidal forcing. All parameters were assigned relatively high initial variances—0.1 $(m/day)^2$ for velocity and 0.4 for admittance and 0.4 $(m/day)^2$ diurnal amplitude—to avoid over-constraining the model and to allow the filter to adaptively adjust based on the observed data.

3. Results

3.1. Along Track Variations

The results of the Kalman filter on the horizontal data are presented in Figure 2, which displays the filtered speed, tidal admittance, and diurnal amplitude, respectively, for the 18 nodes, which gave useable data over time. These are presented alongside data from the tide gauge and air temperature from the weather station in Tasiilaq. Figure 2a clearly demonstrates a progressive increase in velocity as the nodes flow towards the calving front, with a typical acceleration of approximately 0.15 m/day^2.

Tidal admittance varies between nodes but remains relatively stable over time for each individual node, suggesting that the model effectively captures the response to spring–neap tidal cycles (Figure 2b). Most nodes exhibit admittance values between 0.25 and 0.45 (Table 1). The optimal phase offset calculated was for minimum displacement, ~70 min after high tide at the tide gauge.

Most nodes show diurnal amplitude variations in velocity ranging from 0.1 to 0.3 m/day (Table 1, Figure 2c). This results in typical increases of approximately 0.2 m/day in velocity around 14:30 UTC—when surface melt is generally at its peak—and equivalent decreases to a minimum around 02:30 UTC. Similarly, to the tidal admittance, the diurnal amplitude (Figure 2c) remains temporally consistent for each node but exhibits notable between-node spatial variability.

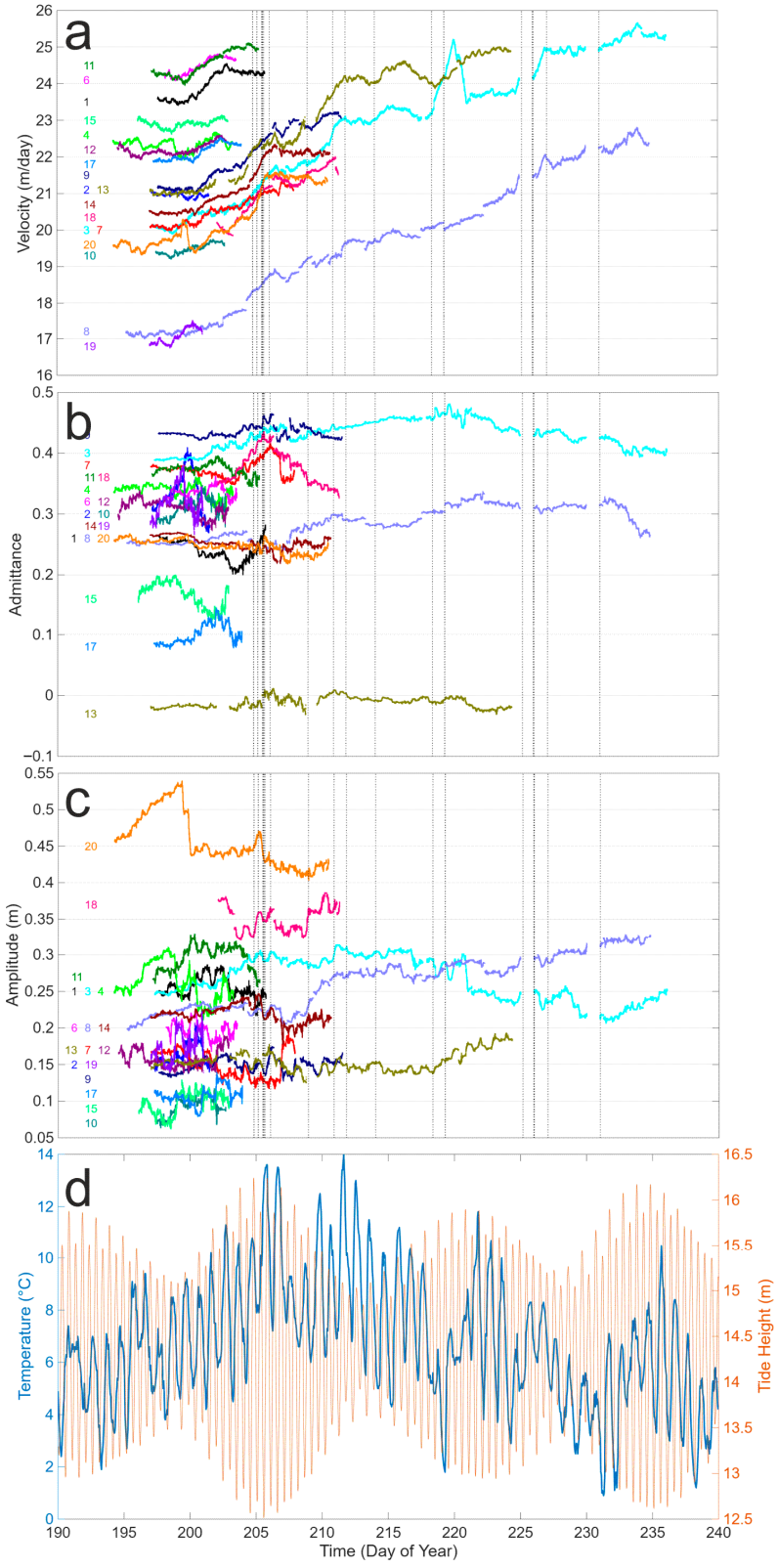

Figure 2. Along-track Kalman Filter output showing: (**a**) Velocity variations over time. (**b**) Tidal admittance variations over time (note that this parameter is unitless). (**c**) Non-tidal diurnal amplitude variations over time. (**d**) Air temperature and tide height. The locations of the weather station at Tasiilaq and the tide gauge are shown in Figure 1. Coloured numbers in (**a**–**c**) indicate node number and are consistent with Figure 3. Dotted vertical lines in (**a**–**c**) indicate calving/glacier earthquake events identified on the cameras (located in Figure 1c) and on the global seismic network as detailed in the supplementary material of [25].

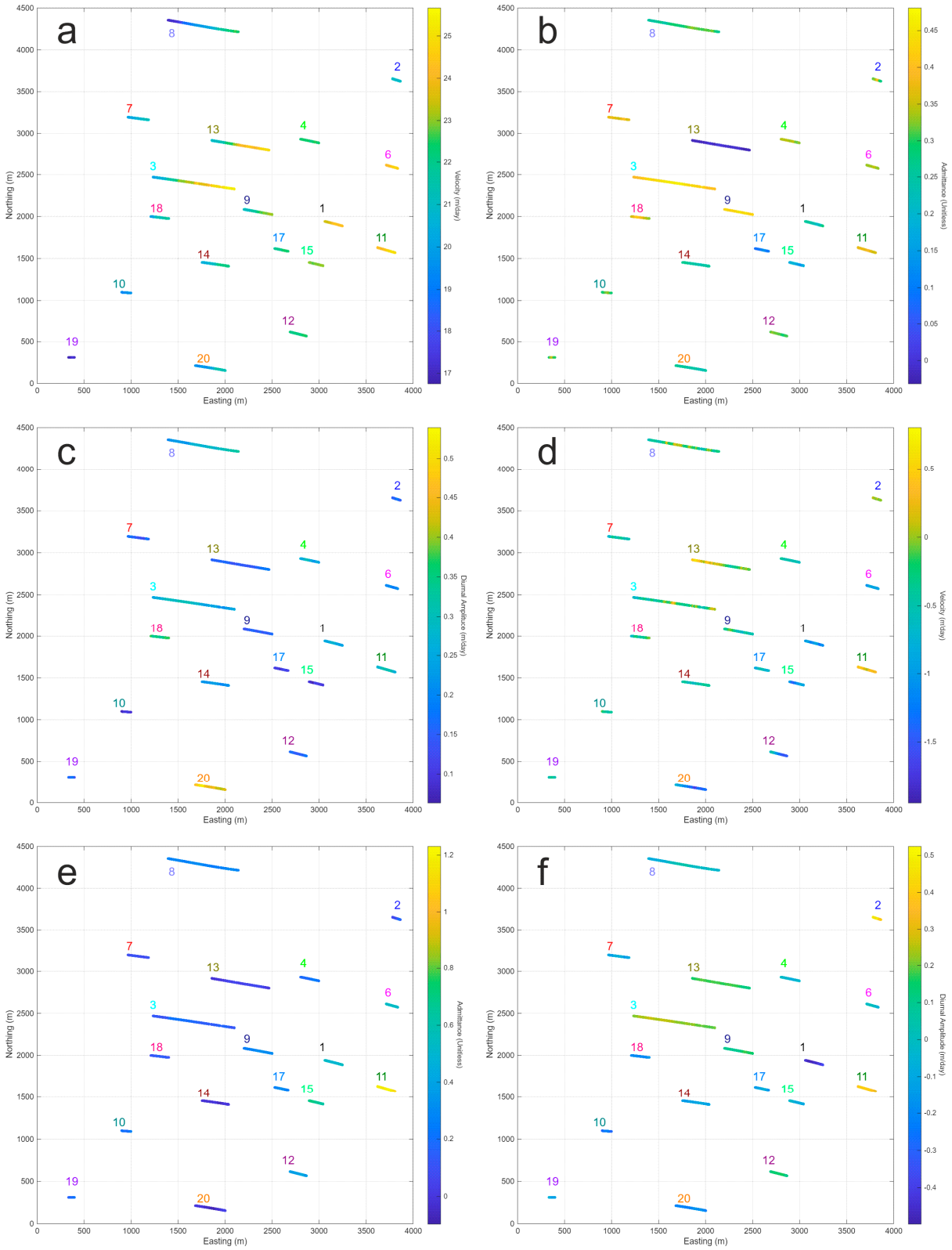

Figure 3. (**a**) Along-track Kalman Filter output showing spatial velocity (m/day) variations. (**b**) Along-track Kalman Filter output showing spatial tidal admittance variations. (**c**) Along-track Kalman Filter output showing spatial diurnal amplitude variations. (**d**) Height Kalman Filter output showing spatial vertical velocity variations. (**e**) Height Kalman Filter output showing spatial admittance variations. (**f**) Height Kalman Filter output showing diurnal amplitude variations. Glacier flows from west to east. Coloured numbers indicate node number and are consistent with Figure 2.

Table 1. Kalman Filter output means and standard deviations. Note that node 5 and node 16 did not produce useful data.

Node Number	Mean Horizontal Tidal Admittance ± Standard Deviation (Unitless)	Mean Vertical Tidal Admittance ± Standard Deviation (Unitless)	Mean Diurnal Amplitude Variation ± Standard Deviation (m/day)	Mean Diurnal Height Amplitude Variation ± Standard Deviation (m/day)
1	0.24 ± 0.02	0.51 ± 0.02	0.26 ± 0.01	-0.45 ± 0.03
2	0.33 ± 0.03	0.11 ± 0.05	0.16 ± 0.01	0.45 ± 0.04
3	0.43 ± 0.02	0.16 ± 0.04	0.27 ± 0.03	0.23 ± 0.02
4	0.34 ± 0.01	0.20 ± 0.02	0.27 ± 0.02	-0.04 ± 0.02
6	0.34 ± 0.01	0.53 ± 0.01	0.20 ± 0.01	-0.01 ± 0.02
7	0.37 ± 0.01	0.09 ± 0.02	0.15 ± 0.02	-0.10 ± 0.03
8	0.28 ± 0.03	0.27 ± 0.02	0.26 ± 0.04	-0.02 ± 0.04
9	0.43 ± 0.01	0.29 ± 0.03	0.15 ± 0.01	0.12 ± 0.04
10	0.31 ± 0.02	0.21 ± 0.02	0.09 ± 0.01	-0.25 ± 0.03
11	0.37 ± 0.01	1.17 ± 0.03	0.29 ± 0.02	0.39 ± 0.02
12	0.31 ± 0.01	0.39 ± 0.02	0.16 ± 0.01	0.14 ± 0.02
13	-0.01 ± 0.01	0.04 ± 0.03	0.15 ± 0.01	0.17 ± 0.02
14	0.25 ± 0.01	-0.01 ± 0.02	0.22 ± 0.01	-0.12 ± 0.02
15	0.17 ± 0.02	0.67 ± 0.03	0.10 ± 0.01	-0.06 ± 0.03
17	0.10 ± 0.02	0.29 ± 0.03	0.11 ± 0.01	-0.11 ± 0.03
18	0.38 ± 0.03	0.13 ± 0.01	0.35 ± 0.02	-0.20 ± 0.01
19	0.32 ± 0.02	0.18 ± 0.02	0.17 ± 0.02	-0.10 ± 0.03
20	0.25 ± 0.01	-0.02 ± 0.03	0.46 ± 0.04	-0.20 ± 0.02

In addition to examining the temporal evolution of the three parameters, their spatial distribution also provides valuable insights (shown in Figure 3). Figure 3a–c depict the spatial patterns of velocity, tidal admittance, and diurnal amplitude, respectively, displaying the 18 working nodes on an Easting–Northing coordinate grid, with colour gradients representing variations in parameter values.

There is a general eastward acceleration towards the calving front, and nodes located near the glacier centre exhibit higher velocities than those positioned near the lateral margins (Figure 3a).

Figure 3b shows the spatial variation in tidal admittance. With the exception of a single outlier (node 13, with near-zero admittance), central nodes tend to exhibit higher admittance values compared to those near the valley sidewalls. No clear relationship, however, is observed between admittance and proximity to the calving front.

Surface meltwater input is expected to cause variation in flow on a diurnal timescale. In contrast to speed and admittance, no consistent spatial trends in diurnal amplitude were apparent (Figure 3c).

3.2. Height Variations

The outputs of the vertical Kalman filter analysis are presented in Figure 3d–f, illustrating vertical velocity, tidal admittance, and diurnal amplitude, respectively. The majority of nodes experienced gradual subsidence, with rates ranging from 0 to 1.5 m/day. Some nodes show uplift during some parts of the observation period—including node 13 and

node 11, the latter lies directly at the glacier terminus. This observation has been previously reported [12] (pp. 964–982) and results from the calving of backward rotating icebergs.

The spatial distribution of the vertical tidal admittance parameter reveals a clear correlation with node position (Figure 3d). Unlike the along-track tidal admittance, which clearly propagated up-glacier (Figure 3b), vertical admittance does not exhibit the same upstream extent (Figure 3e). Nodes within approximately 1 km of the calving front recorded admittance values between 0.4 and 0.7, with the exception of node 11 (1.2) and node 2 (0.2). Nodes further inland are much less impacted in the vertical by tidal forcing.

Figure 3f displays the spatial variation in vertical diurnal amplitude. Across the 18 nodes, the effect is approximately balanced, with an even split between nodes exhibiting positive diurnal signals (daytime uplift) and negative signals (daytime subsidence). Most nodes experienced diurnal amplitudes between −0.2 and 0.2 m/day. Notably, node 1 exhibited a larger negative amplitude (−0.4 m/day), while nodes 2 and 11 recorded positive amplitudes between 0.4 and 0.5 m/day. These three outliers are all located within close proximity to the calving front.

4. Discussion

Variations in marine-terminating glacier flow near the calving margin are known to be controlled by a complex combination of tidal and atmospheric effects alongside iceberg calving, which changes backstress and additionally potentially disrupts the glacier's hydrological system, e.g., [17,31] (pp. 525–540). Separation of these influences will improve our understanding and models of glacier calving and ice discharge, as well as help predictions of glacier response to climatic change.

4.1. Tidally Driven Variations in Glacier Flow

Our along-track tidal admittance values largely lie between +0.25 and +0.45 (Figure 2b) and show that the glacier's flow is slowed at high tide, with flow being retarded by the additional depth of water at the glacier front. This observation is in keeping with observations from Helheim [6] (pp. 1169–1180), [14] (pp. 301–308), [17] and a number of other marine-terminating glaciers in Greenland and Alaska [34] (pp. 8969–8975), [35] (pp. 9051–9058), [36] (pp. 567–578), [37] (pp. 609–621). The optimal phase offset corresponded to the glacier reaching its minimum displacement approximately 70 min after high tide was recorded at the tide gauge. This phase offset compares well with the 2 h, 1.9 h, 1.7 h, and 0 to 4 h delays found by [14] (pp. 301–308), [6] (pp. 1169–1180), [2] (pp. 77–89), [17], respectively. The delay likely reflects both the temporal lag between high tide at the tide gauge and the glacier terminus, as well as the response time of the glacier to tidal forcing.

Our results show that for peak spring tides (~1.5 m), the glacier velocity reduction is approximately 0.375–0.675 m/day from the mean at high tide, with a comparable increase at low tide. During peak neap tides (~0.5 m), the variation is reduced to approximately 0.125–0.225 m/day. Our admittance values are significantly greater than the 0.028 and 0.026–0.079 found by [6] (pp. 1169–1180), [17], respectively, at Helheim Glacier. However, most of those results were taken significantly further upglacier, varying between ~37 km and ~1.5 km from the glacier front. De Juan et al. [17] further showed that tidal admittance increased significantly towards the glacier margin and that glacier calving caused an increase in tidal admittance.

Nodes located close to the centre line of the glacier tend to exhibit higher along-track admittance values compared to those near the glacier margins (Figure 3b), with the exception of a single outlier (node 13, with near-zero admittance), meaning that the effect of the tides is felt more at the glacier centre than near the valley walls. This observation

aligns with physical expectations, as lateral drag from valley walls is likely to dampen the glacier's response to tidal forcing. No clear relationship, however, is observed between admittance and proximity to the calving front, meaning the effects propagate significantly up the glacier over the length scales of this experiment (~3 km).

In contrast, the spatial distribution of the vertical tidal admittance parameter reveals a clear correlation with node position (Figure 3e). These admittance values correspond to uplift magnitudes of approximately 0.6–1.05 m during high spring tides and 0.2–0.35 m during high neap tides, with comparable subsidence observed at low tide. Except close to the calving margin (approximately the final km), all nodes exhibited admittance values below 0.4, indicating that vertical motion becomes increasingly dampened with distance from the calving front, which is consistent with the glacier front being lightly grounded. Nodes 11 and 2, both located at the calving front, may have been subject to rotational motions during calving events [12] (pp. 964–982), [25] (pp. 205–308), potentially accounting for their anomalous behaviour.

4.2. Diurnally Driven Flow Variations

Our results show a general eastward acceleration in flowrates towards the calving front, and nodes located near the glacier centre exhibit higher velocities than those positioned near the lateral margins (Figure 3a). This distribution is consistent with well-established glaciological patterns of ice flow (as established by early pioneers Agassiz and Tyndall, e.g., Ref. [38]), providing further validation of the Kalman filter's capability to capture known spatial dynamics.

On many glaciers, the arrival of surface meltwater at the bed facilitates variations in glacier sliding and hence flowrate, with typically faster flow lagging peak melt. Most of our GPS nodes showed diurnal variations in velocity ranging from 0.1 to 0.3 m/day, with flow speed peaking around 3.5 h after local noon. The magnitude of the diurnal variation in horizontal speed does not show much spatial or temporal variability (Figure 3c). The absence of a clear pattern may reflect the length scales of the experiment being smaller than any spatial variability. The diurnal speed variations we observe align well with the variation of 0.35 m/day and 0.25–0.4 m/day found by Davis et al. [6] (pp. 1169–1180), and Stevens et al. [2] (pp. 77–89), respectively. Sugiyama et al. [31] (pp. 525–540) also observed diurnal signals to vary consistently over their study area. [6] (pp. 1169–1180) found maximum velocity due to diurnal variations to be 6 h after local noon (17:00 UTC), and Stevens et al. [2] (pp. 77–89) found the peak to be at 21:00 UTC, which is later than the speed peaks we observe. Lag times for velocity-meltwater interactions are known to vary through the melt season, with lag times being significantly higher early in the melt season than later (e.g., Ref. [39]).

Concomitant with variations in horizontal flow speed, diurnal vertical uplift can occur if the glacier's water system is overwhelmed by the arrival of surface water at the bed. This is the most common in spring as the water system develops. Further, since our nodes were sitting directly on the glacier surface, surface melt would be expected to cause a diurnal signal of daytime subsidence during warm daylight hours. Across the 18 GPS nodes we installed on Helheim, there was an even split between nodes exhibiting positive diurnal signals (daytime uplift) and negative signals (daytime subsidence), suggesting both effects may be in play. Most nodes experienced diurnal amplitudes between -0.2 and 0.2 m/day. Notably, node 1 exhibited a larger negative amplitude (-0.4 m/day), while nodes 2 and 11 recorded positive amplitudes between 0.4 and 0.5 m/day. These three outliers are all located within close proximity to the calving front, suggesting that localised dynamic processes—potentially linked to calving-induced rotation, crevasse formation, or surface instabilities—may have influenced the observed diurnal vertical responses.

5. Conclusions

To investigate short-term velocity variations near the calving margin of Helheim Glacier, we analysed GPS records from 18 nodes installed very close to the glacier's calving front during July and August 2013. Our results show that tidally driven vertical displacements are limited to the final kilometre or so of the glacier. In contrast, the horizontal flow speed of the glacier is modulated by the tides, especially at the centre of the glacier, over distances of at least several kilometres. Tidal admittance values largely lie between +0.25 and +0.45 (Figure 2b) and show that the glacier's flow is slowed at high tide, with minimum displacement occurring ~70 min after high tide. Diurnal variations in horizontal speed, driven by atmospheric temperature, vary much less spatially and temporally, with most nodes experiencing changes from the mean speed of ±0.1–0.3 m/day, with the fastest flow approximately 3.5 h after local noon. Even so, the findings demonstrate that surface meltwater does influence glacier margin dynamics. Together, the results highlight the need to incorporate complex short-period external forcings into predictive models of marine-terminating glacier behaviour.

Author Contributions: All authors have contributed significantly to this research. Data curation, C.P.; Funding acquisition, T.M. and S.E.; Investigation, T.M. and S.E.; Methodology, C.P., J.C., T.M. and S.E.; Project administration, T.M. and S.E.; Resources, S.E.; Supervision, C.P., T.M. and S.E.; Writing—original draft, C.P. and T.M.; Writing—review and editing, T.M. and S.E. All authors have read and agreed to the published version of the manuscript.

Funding: This research was funded by UK NERC, grant number NE/I007148/1. C.P. was funded by Newcastle University.

Institutional Review Board Statement: Not applicable.

Informed Consent Statement: Not applicable.

Data Availability Statement: The original data presented in the study are openly available in FigShare at https://figshare.com/articles/dataset/Helheim_Node_data/29491607. Data deposited 10 July 2025.

Conflicts of Interest: The authors declare no conflicts of interest. The funders had no role in the design of the study; in the collection, analyses, or interpretation of data; in the writing of the manuscript; or in the decision to publish the results.

References

1. Bartholomaus, T.C.; Larsen, C.F.; West, M.E.; O'Neel, S.; Pettit, E.C.; Truffer, M. Tidal and seasonal variations in calving flux observed with passive seismology. *J. Geophys. Res. Earth Surf.* **2015**, *120*, 2318–2337. [CrossRef]
2. Stevens, L.A.; Nettles, M.; Davis, J.L.; Creyts, T.T.; Kingslake, J.; Ahlstrom, A.P.; Larsen, T.B. Helheim Glacier diurnal velocity fluctuations driven by surface melt forcing. *J. Glaciol.* **2022**, *68*, 77–89. [CrossRef]
3. Luckman, A.; Benn, D.I.; Cottier, F.; Bevan, S.; Nilsen, F.; Inall, M. Calving rates at tidewater glaciers vary strongly with ocean temperature. *Nat. Commun.* **2015**, *6*, 8566. [CrossRef]
4. O'Leary, M.; Christoffersen, P. Calving on tidewater glaciers amplified by submarine frontal melting. *Cryosphere* **2013**, *7*, 119–128. [CrossRef]
5. Vaňková, I.; Holland, D.M. Calving signature in ocean waves at Helheim Glacier and Sermilik Fjord, East Greenland. *J. Phys. Oceanogr.* **2016**, *46*, 2925–2941. [CrossRef]
6. Davis, J.L.; De Juan, J.; Nettles, M.; Elosegui, P.; Andersen, M.L. Evidence for non-tidal diurnal velocity variations of Helheim Glacier, East Greenland. *J. Glaciol.* **2014**, *60*, 1169–1180. [CrossRef]
7. Marsh, O.J.; Rack, W.; Floricioiu, D.; Golledge, N.R.; Lawson, W. Tidally induced velocity variations of the Beardmore Glacier, Antarctica, and their representation in satellite measurements of ice velocity. *Cryosphere* **2013**, *7*, 1375–1384. [CrossRef]
8. Murray, T.; Smith, A.M.; King, M.A.; Weedon, G.P. Ice flow modulated by tides at up to annual periods at Rutford Ice Stream, West Antarctica. *Geophys. Res. Lett.* **2007**, *34*, L18503. [CrossRef]
9. O'Neel, S.; Echelmeyer, K.A.; Motyka, R.J. Short-term variations in calving of a tidewater glacier: LeConte Glacier, Alaska, U.S.A. *J. Glaciol.* **2003**, *49*, 587–598. [CrossRef]

10. Schild, K.M.; Hamilton, G.S. Seasonal variations of outlet glacier terminus position in Greenland. *J. Glaciol.* **2013**, *59*, 759–770. [CrossRef]
11. Mouginot, J.; Rignot, E.; Bjørk, A.A.; Van den Broeke, M.; Millan, R.; Morlighem, M.; Noël, B.; Scheuchl, B.; Wood, M. Forty-six years of Greenland Ice Sheet mass balance from 1972 to 2018. *Proc. Natl. Acad. Sci. USA* **2019**, *116*, 9239–9244. [CrossRef]
12. Murray, T.; Selmes, N.; James, T.D.; Edwards, S.; Martin, I.; O'Farrell, T.; Aspey, R.; Rutt, I.; Nettles, M.; Baugé, T. Dynamics of glacier calving at the ungrounded margin of Helheim Glacier, southeast Greenland. *J. Geophys. Res. Earth Surf.* **2015**, *120*, 964–982. [CrossRef]
13. De Juan, J. *Tidewater Glacier Flow of Helheim Glacier, Greenland, 2006–2008, Using High-Rate GPS*; PhD, Universitat De Barcelona: Barcelona, Spain, 2011. Available online: http://hdl.handle.net/10803/79173 (accessed on 23 December 2025).
14. Voytenko, D.; Stern, A.; Holland, D.M.; Dixon, T.H.; Christianson, K.; Walker, R.T. Tidally driven ice speed variation at Helheim Glacier, Greenland, observed with terrestrial radar interferometry. *J. Glaciol.* **2015**, *61*, 301–308. [CrossRef]
15. Stevens, L.A.; Nettles, M.; Davis, J.L.; Creyts, T.T.; Kingslake, J.; Hewitt, I.J.; Stubblefield, A. Tidewater-glacier response to supraglacial lake drainage. *Nat. Commun.* **2022**, *13*, 6065. [CrossRef]
16. Martin, I.; O'Farrell, T.; Aspey, R.; Edwards, S.; James, T.; Loskot, P.; Murray, T.; Rutt, I.; Selmes, N.; Baugé, T. A high-resolution sensor network for monitoring glacier dynamics. *IEEE Sens. J.* **2014**, *14*, 3926–3931. [CrossRef]
17. De Juan, J.; Elósegui, P.; Nettles, M.; Larsen, T.B.; Davis, J.L.; Hamilton, G.S.; Stearns, L.A.; Andersen, M.L.; Ekström, G.; Ahlstrøm, A.P.; et al. Sudden increase in tidal response linked to calving and acceleration at a large Greenland outlet glacier. *Geophys. Res. Lett.* **2010**, *37*, L12501. [CrossRef]
18. Cheng, G.; Morlighem, M.; Mouginot, J.; Cheng, D. Helheim Glacier's terminus position controls its seasonal and inter-annual ice flow variability. *Geophys. Res. Lett.* **2022**, *49*, e2021GL097085. [CrossRef]
19. Rignot, E.; Kanagaratnam, P. Changes in the velocity structure of the Greenland ice sheet. *Science* **2006**, *311*, 986–990. [CrossRef] [PubMed]
20. Murray, T.; Scharrer, K.; James, T.D.; Dye, S.R.; Hanna, E.; Booth, A.D.; Selmes, N.; Luchman, A.; Hughes, A.L.C.; Cook, S.; et al. Ocean regulation hypothesis for glacier dynamics in southeast Greenland and implications for ice sheet mass changes. *J. Geophys. Res.* **2010**, *115*, F03026. [CrossRef]
21. Straneo, F. (University of California, San Diego, CA, USA). Personal Communication, 2024.
22. Bevan, S.L.; Luckman, A.; Khan, S.A.; Murray, T. Seasonal dynamic thinning at Helheim Glacier. *Earth Planet. Sci. Lett.* **2015**, *415*, 47–53. [CrossRef]
23. Ekström, G.; Nettles, M.; Abers, G.A. Glacial Earthquakes. *Science* **2003**, *302*, 622–624. [CrossRef]
24. Tsai, V.C.; Ekström, G. Analysis of glacial earthquakes. *J. Geophys. Res.* **2007**, *112*, F03S22. [CrossRef]
25. Murray, T.; Nettles, M.; Selmes, N.; Cathles, L.M.; Burton, J.C.; James, T.D.; Edwards, S.; Martin, I.; O'Farrell, T.; Aspey, R.; et al. Reverse glacier motion during iceberg calving and the cause of glacial earthquakes. *Science* **2015**, *349*, 305–308. [CrossRef]
26. Ekström, G.; Nettles, M.; Tsai, V.C. Seasonality and increasing frequency of Greenland glacial earthquakes. *Science* **2006**, *311*, 1756–1758. [CrossRef]
27. Veitch, S.A.; Nettles, M. Spatial and Temporal Variations in Greenland Glacial-Earthquake Activity, 1993–2010. *J. Geophys. Res.* **2012**, *117*, F04007. [CrossRef]
28. Olsen, K.G.; Nettles, M. Patterns in glacial-earthquake activity around Greenland, 2011–2013. *J. Glaciol.* **2017**, *63*, 1077–1089. [CrossRef]
29. Kehrl, L.M.; Joughin, I.; Shean, D.E.; Floricioiu, D.; Krieger, L. Seasonal and interannual variabilities in terminus position, glacier velocity, and surface elevation at Helheim and Kangerlussuaq Glaciers from 2008 to 2016. *J. Geophys. Res. Earth Surf.* **2017**, *122*, 1635–1652. [CrossRef]
30. Andersen, M.L.; Nettles, M.; Elosegui, P.; Larson, T.B.; Hamilton, G.S.; Stearns, L.A. Quantitative estimates of velocity sensitivity to surface melt variations at a large Greenland outlet glacier. *J. Glaciol.* **2011**, *57*, 609–620. [CrossRef]
31. Sugiyama, S.; Tsutaki, S.; Sakakibara, D.; Asaji, I.; Kondo, K.; Wang, Y.; Podolskiy, E.; Jouvet, G.; Funk, M. Ice speed of a Greenlandic tidewater glacier modulated by tide, melt, and rain. *Cryosphere* **2025**, *19*, 525–540. [CrossRef]
32. Chen, G. *GPS Kinematic Positioning for the Airborne Laser Altimetry at Long Valley, California*; PhD, MiT: Cambridge, MA, USA, 1998; Available online: https://dspace.mit.edu/handle/1721.1/9680 (accessed on 23 December 2025).
33. Kalman, R.E. A New Approach to Linear Filtering and Prediction Problems. *J. Basic Eng.* **1960**, *82*, 35–45. [CrossRef]
34. Walters, R.A.; Dunlap, W.W. Analysis of time series of glacier speed: Columbia Glacier, Alaska. *J. Geophys. Res. Solid Earth* **1987**, *92*, 8969–8975. [CrossRef]
35. Meier, M.F.; Post, A. Fast tidewater glaciers. *J. Geophys. Res.* **1987**, *92*, 9051–9058. [CrossRef]
36. O'Neel, S.; Echelmeyer, K.; Motyka, R. Short-term flow dynamics of a retreating tidewater glacier: LeConte Glacier, Alaska, U.S.A. *J. Glaciol.* **2001**, *47*, 567–578. [CrossRef]
37. Podrasky, D.; Truffer, M.; Lüthi, M.; Fahnestock, M. Quantifying velocity response to ocean tides and calving near the terminus of Jakobshavn Isbræ, Greenland. *J. Glaciol.* **2014**, *60*, 609–621. [CrossRef]

38. Waddington, E.D. Life, death and afterlife of the extrusion flow theory. *J. Glaciol.* **2010**, *56*, 973–996. [CrossRef]
39. Cuffey, K.M.; Paterson, W.S.B. *The Physics of Glaciers*, 4th ed.; Academic Press: Amsterdam, The Netherlands, 2010; 704p, ISBN 978-0-123-69461-4.